

Entanglement-enhanced matter-wave interferometry in a high-finesse cavity

<https://doi.org/10.1038/s41586-022-05197-9>

Graham P. Greve^{1,2}, Chengyi Luo^{1,2}, Baochen Wu¹ & James K. Thompson^{1✉}

Received: 26 October 2021

Accepted: 5 August 2022

Published online: 19 October 2022

Open access

 Check for updates

An ensemble of atoms can operate as a quantum sensor by placing atoms in a superposition of two different states. Upon measurement of the sensor, each atom is individually projected into one of the two states. Creating quantum correlations between the atoms, that is entangling them, could lead to resolutions surpassing the standard quantum limit^{1–3} set by projections of individual atoms. Large amounts of entanglement^{4–6} involving the internal degrees of freedom of laser-cooled atomic ensembles^{4–16} have been generated in collective cavity quantum-electrodynamics systems, in which many atoms simultaneously interact with a single optical cavity mode. Here we report a matter-wave interferometer in a cavity quantum-electrodynamics system of 700 atoms that are entangled in their external degrees of freedom. In our system, each individual atom falls freely under gravity and simultaneously traverses two paths through space while entangled with the other atoms. We demonstrate both quantum non-demolition measurements and cavity-mediated spin interactions for generating squeezed momentum states with directly observed sensitivity $3.4^{+1.1}_{-0.9}$ dB and $2.5^{+0.6}_{-0.6}$ dB below the standard quantum limit, respectively. We successfully inject an entangled state into a Mach–Zehnder light-pulse interferometer with directly observed sensitivity $1.7^{+0.5}_{-0.5}$ dB below the standard quantum limit. The combination of particle delocalization and entanglement in our approach may influence developments of enhanced inertial sensors^{17,18}, searches for new physics, particles and fields^{19–23}, future advanced gravitational wave detectors^{24,25} and accessing beyond mean-field quantum many-body physics^{26–30}.

Light-pulse matter-wave interferometers exploit the quantized momentum kick given to atoms during absorption and emission of light to split atomic wave packets so that they traverse distinct spatial paths at the same time. Additional momentum kicks then return the atoms to the same point in space to interfere the two matter-wave wave packets. The key to the precision of these devices is the encoding of information in the phase ϕ that appears in the superposition of the two quantum trajectories within the interferometer. This phase must be estimated from quantum measurements to extract the desired information. For N atoms, the phase estimation is fundamentally limited by the independent quantum collapse of each atom to an r.m.s. angular uncertainty $\Delta\theta_{\text{SQL}} = 1/\sqrt{N}$ rad, known as the standard quantum limit (SQL)².

Here we demonstrate a matter-wave interferometer^{31,32} with a directly observed interferometric phase noise below the SQL, a result that combines two of the most striking features of quantum mechanics: the concept that a particle can appear to be in two places at once and entanglement between distinct particles. This work is also a harbinger of future quantum many-body simulations with cavities^{26–29} that will explore beyond mean-field physics by directly modifying and probing quantum fluctuations or in which the quantum measurement process induces a phase transition³⁰.

Quantum entanglement between the atoms allows the atoms to conspire together to reduce their total quantum noise relative to their total

signal^{1,3}. Such entanglement has been generated between atoms using direct collisional^{33–39} or Coulomb^{40,41} interactions, including relative atom number squeezing between matter waves in spatially separated traps^{33,35,39} and mapping of internal entanglement onto the relative atom number in different momentum states⁴². A trapped matter-wave interferometer with relative number squeezing was realized in ref. ³⁵, but the interferometer's phase was antisqueezed and thus the phase resolution was above the SQL.

We report the generation of cavity quantum-electrodynamics entanglement between the external momentum states of different atoms using two distinct approaches that both rely on the strong collective coupling between the atoms and an optical cavity. In the first approach, we realize cavity-enhanced quantum non-demolition (QND) measurements^{4,5,7,8} to essentially measure and subtract out the quantum noise. In the second approach, we use the cavity to mediate unitary interactions between the atoms to realize so-called one-axis twisting (OAT)^{1,14–16,43} or an all-to-all Ising interaction. Both approaches have been realized for generating as much as 18.5 dB of entanglement^{4,5}, but only between internal states of atoms and with only the realization of directly observed enhancements in entangled microwave clocks^{12,13} and magnetometers⁴⁴. Cavity approaches to OAT⁴⁵ and QND⁴⁶ entanglement of purely Bragg interferometers have also been proposed.

¹JILA, NIST and Department of Physics, University of Colorado, Boulder, CO, USA. ²These authors contributed equally: Graham P. Greve, Chengyi Luo. ✉e-mail: jkt@jila.colorado.edu

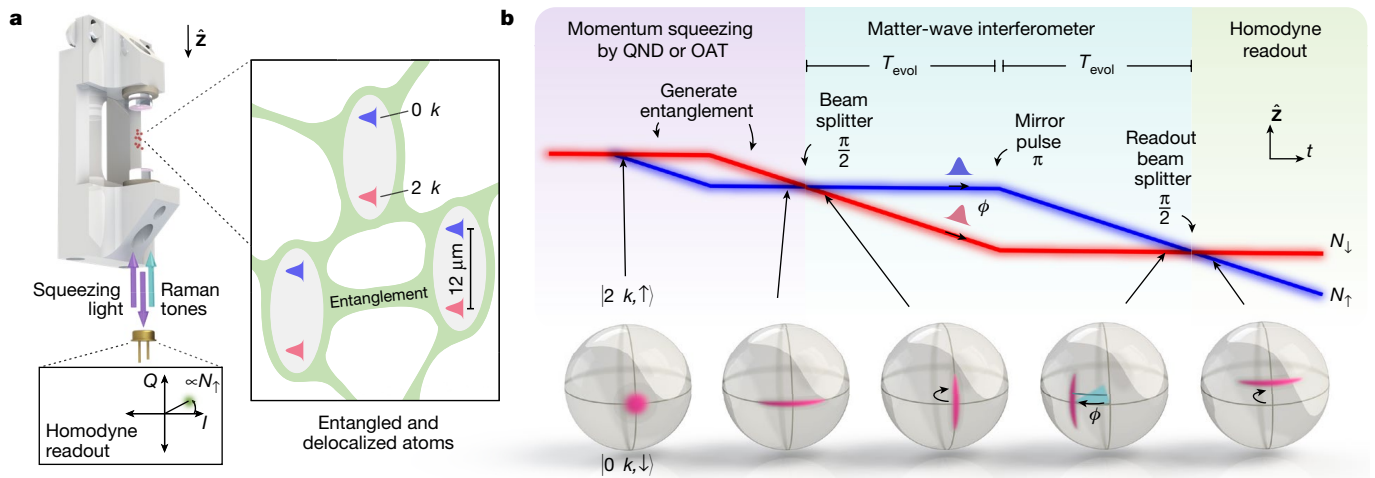


Fig. 1 | Experimental overview. **a**, Ultracold atoms undergo guided free fall in a vertical high-finesse cavity. The atomic wave packets are split and recombined by driving two-photon Raman transitions to provide quantized momentum kicks to the atoms. Intracavity atomic probe light (right inset) generates entanglement between the atoms by either OAT dynamics or QND measurements made by detecting (bottom inset) the reflected atomic probe field's Q quadrature with a homodyne detector^{5,47}. The entanglement between atoms is seen to persist over wave packet separations exceeding 12 μm . **b**, Space-time and Bloch sphere depictions of the generation and injection of

the entanglement into a Mach-Zehnder matter-wave interferometer. Squeezing is first generated in the population basis, and then a Raman beam splitter pulse orients the squeezing for enhanced interferometer phase sensitivity. The two paths (red and blue) accrue a relative phase ϕ over time $2T_{\text{evol}}$, the mirror pulse serves to re-overlap the wave packets and the readout beam splitter pulse creates interference that is read out as a population difference with sub-SQL sensitivity. Representative noise distributions are depicted on the Bloch sphere for various points in the interferometer.

Strong collective coupling to the cavity $NC \gg 1$ is the key requirement for both approaches to generate entanglement, where C is the single particle cooperativity parameter^{43,47,48}. Previously, an interferometer was operated in a low finesse cavity^{49,50}, to provide power build-up, spatial mode filtering and precise beam alignment. Here we achieve matter-wave interferometric control^{31,32} simultaneously with strong collective coupling $NC \approx 500$ by operating inside a cavity with high finesse $\mathcal{F} = 1.3 \times 10^5$ with small mode waist $w_0 = 72 \mu\text{m}$.

Our two-mirror cavity is vertically oriented along \hat{Z} (Fig. 1). The cavity has a power decay rate $\kappa = 2\pi \times 56(3)$ kHz at 780 nm, a mirror separation $L = 2.2$ cm and a free spectral range $\omega_{\text{FSR}} = 2\pi \times 6.7879$ GHz (all error bars reported are 1σ uncertainties). Rubidium atoms are laser cooled inside the cavity and then allowed to fall under gravity for a duration of T_{fall} , guided tightly along the cavity axis by a hollow (Laguerre-Gauss LG_{01} -like) blue-detuned optical dipole guide⁵¹ with thermal r.m.s. cloud transverse radius of $r_{\text{r.m.s.}} = 4.7(8) \mu\text{m} \ll w_0$ (Methods).

Manipulating matter waves

We manipulate matter-wave wave packets using velocity-sensitive two-photon transitions with wavelength $\lambda = 780$ nm. The combined absorption and stimulated emission of photons imparts $2\hbar k$ momentum kicks oriented along the cavity axis, where $k = 2\pi/\lambda$ and \hbar is the reduced Planck constant.

For Raman transitions in which both momentum and spin states are changed, we use the magnetically insensitive ⁸⁷Rb clock states, $|\downarrow\rangle \equiv |F=1, m_F=0\rangle$ and $|\uparrow\rangle \equiv |F=2, m_F=0\rangle$, separated by the hyperfine transition frequency $\omega_{\text{HF}} \approx 2\pi \times 6.835$ GHz. The driving laser's frequency is stabilized between two TEM₀₀ longitudinal modes approximately $\Delta = 2\pi \times 85$ GHz blue-detuned of $|\uparrow\rangle \rightarrow |e\rangle \equiv |5^2P_{3/2}, F=3\rangle$ (Fig. 2a). As shown in Fig. 2b, the cavity free spectral range is tuned such that two sidebands at $\pm\omega_r$ are approximately $\pm 2\pi \times 23$ MHz from resonance with the closest TEM₀₀ mode when $2\omega_r = \omega_{\text{HF}}$. This configuration allows enough light to non-resonantly enter the cavity for a two-photon Rabi frequency $\Omega_{\text{TwoPh}} = 2\pi \times 10$ kHz. By injecting the Raman tones non-resonantly and with opposite detunings, we greatly suppress laser

frequency noise from being converted into phase and amplitude noise inside the cavity. Such noise manifests as noise in the Raman rotations and undesired Bragg scattering to other momentum states. The frequency difference of the sidebands is linearly ramped at a rate of 25 kHz ms^{-1} to compensate for the acceleration of the atoms by gravity (Methods).

In Fig. 2c, we show the initial axial velocity spectrum of the atoms as mapped out by inducing velocity-dependent spin flips. We use this same process to select atoms within a narrow range of initial velocities for coherent manipulation of matter waves, resulting in approximately $N_0 = 800$ – $1,200$ atoms in $|\downarrow\rangle$ with r.m.s. momentum spread $\Delta p = 0.1\hbar k$ set by choice of the two-photon Rabi frequency $\Omega_{\text{TwoPh}} = 2\pi \times 1.4$ kHz (Methods).

In Fig. 2d, we demonstrate the quantized nature of the momentum kicks imparted by the intracavity Raman transitions. After velocity selection, a $\pi/2$ pulse is followed by a second Raman π pulse to place the atoms into a superposition of $|0\hbar k, \downarrow\rangle$ and $|4\hbar k, \downarrow\rangle$ in the falling frame of reference. We observe this as two distinct peaks separated in the subsequent velocity spectrum. Future interferometers might evolve in such superpositions so as to minimize systematic errors and dephasing due to differential environmental couplings to $|\uparrow\rangle$ and $|\downarrow\rangle$.

Complementary to hyperfine spin-state changing Raman transitions, we also demonstrate intracavity Bragg transitions in this high-finesse and high-cooperativity cavity. The Bragg coupling (Methods) connects states $|n\hbar k\rangle \leftrightarrow |(n+2)\hbar k\rangle$ with no change in the spin degree of freedom, as shown in Fig. 2e. After velocity selection, the wave packet is coherently split by a Bragg $\pi/2$ pulse, followed by successive π pulses to transfer momentum to one of the wave packet components for a momentum difference of up to $10\hbar k$. Access to Bragg transitions opens the door to both large momentum transfer operations for greater sensitivity and to improved coherence times in future work.

Squeezing on momentum states

We now turn our attention to creating entanglement between atoms that includes this external degree of freedom. We describe the

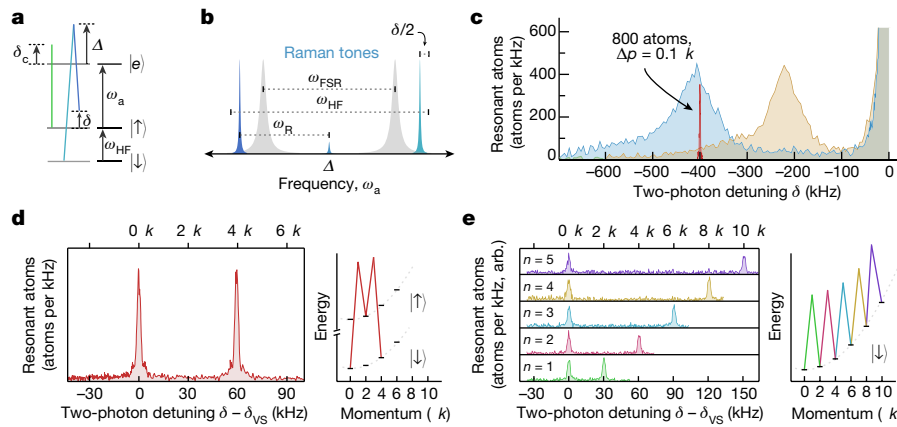


Fig. 2 | Manipulating matter waves in a high-finesse cavity. **a**, Simplified energy-level diagram for ^{87}Rb . The empty-cavity resonance used for probing (green) is detuned by δ_c from the $|\uparrow\rangle \rightarrow |e\rangle$ transition ω_a . The Raman tones (blue) injected into the cavity drive a spin-changing $|\uparrow\rangle \leftrightarrow |\downarrow\rangle$ transition with two-photon detuning δ defined in a falling reference frame. **b**, The Raman tones are derived from a laser detuned Δ from ω_a , locked between two adjacent TEM₀₀ modes separated by ω_{FSR} (grey), and modulated at $\omega_R \approx \omega_{\text{HF}}/2$ for ground-state hyperfine splitting ω_{HF} , leaving the tones detuned from the cavity resonances by ± 23 MHz. **c**, Atoms are prepared in $|\downarrow\rangle$ and allowed to fall for a duration of $T_{\text{fall}} = 7.5$ ms (orange) or 15 ms (blue). The Raman coupling is applied at a fixed detuning δ , after which the number of atoms in $|\uparrow\rangle$ is measured, revealing the axial velocity distribution. The full-width half-maximum of both distributions

corresponds to a momentum spread of $5\hbar k$, which is too broad for interferometry. During velocity selection, a group of about 800 atoms with r.m.s. momentum spread $\Delta p = 0.1\hbar k$ (red) are kept from the latter distribution whereas the rest are removed with transverse radiation pressure. **d**, After velocity selection at a two-photon detuning δ_{vs} , a pair of Raman transitions can be used to place atoms into a superposition of $|0\hbar k, \downarrow\rangle$ and $|4\hbar k, \downarrow\rangle$. Raman spectroscopy is used to verify the discrete velocity distribution. **e**, Alternatively, Bragg transitions can be driven by adding amplitude modulation to the Raman tones. Here a Bragg $\pi/2$ pulse splits the wave packet, and consecutive π pulses transfer additional momentum to create a superposition $|0\hbar k, \downarrow\rangle$ and $|2n\hbar k, \downarrow\rangle$ with the momentum difference as large as $10\hbar k$ shown here.

collective state of our matter-wave interferometer using a Bloch sphere with average Bloch vector $\mathbf{J} = \langle \hat{J}_x \hat{\mathbf{x}} + \hat{J}_y \hat{\mathbf{y}} + \hat{J}_z \hat{\mathbf{z}} \rangle$ of length $J = \|\mathbf{J}\| \leq N_0/2$ in a fictitious coordinate space (Fig. 1b). The collective pseudospin projection operators are defined as $\hat{J}_z \equiv \frac{1}{2}(\hat{N}_\uparrow - \hat{N}_\downarrow)$ with collective population projection operators $\hat{N}_\uparrow = \sum_i^{N_0} |a\rangle_i \langle a|$ and $\hat{N}_\downarrow = \sum_i^{N_0} |b\rangle_i \langle b|$, and similarly for other pseudospin projections, where $|a\rangle_i = |2\hbar k, \uparrow\rangle_i$ and $|b\rangle_i = |0\hbar k, \downarrow\rangle_i$ for the i th atom. We use a Raman $\pi/2$ pulse to nominally prepare all atoms in an unentangled coherent pseudospin state described by the Bloch vector $\mathbf{J} = J\hat{\mathbf{x}}$. The SQL arises from the non-zero variance of the spin projection operators $(\Delta J_z)^2 = \langle \hat{J}_z^2 \rangle - \langle \hat{J}_z \rangle^2 \neq 0$, and so on, and is visualized on the Bloch sphere as a quasiprobability distribution of the orientation of the Bloch vector from trial to trial. We prepare squeezed momentum states using both QND measurements^{4,5,47} and OAT^{1,14,43} in which the quantum noise is reduced in one spin-momentum projection at the expense of increased quantum noise along the orthogonal projection.

The Wineland parameter W characterizes the phase enhancement of a squeezed state with phase uncertainty $\Delta\theta$ that is certified to arise from entanglement between the atoms³,

$$W = \left(\frac{\Delta\theta}{\Delta\theta_{\text{SQL}}} \right)^2. \quad (1)$$

Physically, W is the reduction in the angular noise variance of the phase estimation relative to the SQL, $\Delta\theta_{\text{SQL}} = 1/\sqrt{N}$, one would have for a pure state with a Bloch vector length $J_c = N/2$ equal to that of the actual mixed or partially decohered state prepared without the squeezing operation (Methods).

Collective QND measurements of the free falling atomic samples are used to estimate the number of atoms in different spin-momentum states without revealing single-particle information^{47,51}. The two momentum states interact differently with the optical cavity because they carry distinct spin labels. We tune a TEM₀₀ cavity mode with resonance frequency ω_c to the blue of the $|\uparrow\rangle \rightarrow |e\rangle$ transition ω_a by $\delta_c = \omega_c - \omega_a$ (Fig. 2a). After adiabatically eliminating the excited state $|e\rangle$ and ignoring mean-field

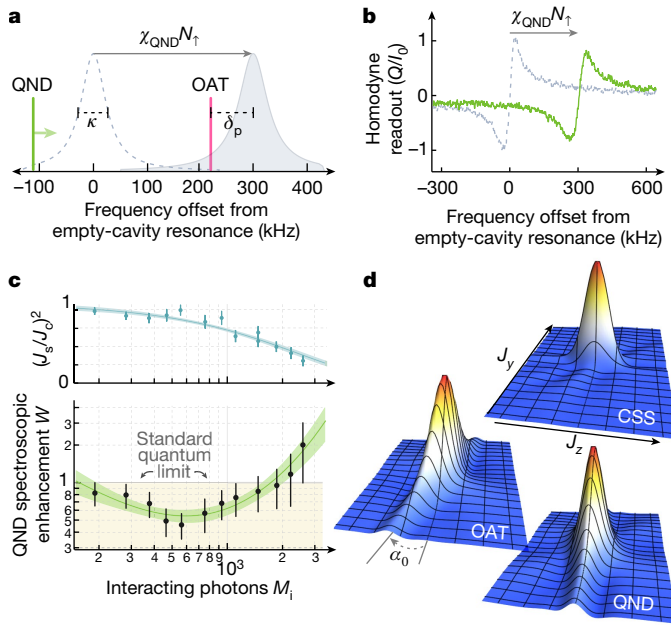
light shifts that will be spin-echoed away, the effective Hamiltonian⁴³ describing the atom-cavity QND interaction can be expressed in a rotating frame at the atomic transition frequency as

$$\hat{\mathcal{H}}_{\text{QND}} = \hbar(\delta_c + \chi_{\text{QND}} \hat{N}_\uparrow) \hat{c}^\dagger \hat{c} \quad (2)$$

where the cavity field is described by creation and annihilation operators \hat{c}^\dagger and \hat{c} . The cavity resonance shifts by an amount $\chi_{\text{QND}} = 2\pi \times 335(4)$ Hz per atom in $|\uparrow\rangle$ at a detuning $\delta_c = 2\pi \times 175$ MHz (Methods). The population N_\uparrow of atoms in the momentum state with spin label $|\uparrow\rangle$ can be estimated by measuring the cavity frequency shift, which is estimated by detecting the probe light reflected from the cavity input mirror as the laser frequency is swept across resonance (Figs. 1a and 3a,b). A typical measurement lasts 150 μs . The population N_\downarrow of atoms in the momentum state with spin label $|\downarrow\rangle$ is measured with the same technique after transferring the atoms to $|\uparrow\rangle$ using a Raman π pulse. The Raman π pulse serves the additional functions of re-overlapping the wave packets and cancelling the average light shift of the probe.

Collective QND measurements are used in creating conditional spin squeezing. The spin-momentum projection in the population basis is measured once with the pre-measurement outcome $J_{z\text{p}} = \frac{1}{2}(N_\uparrow - N_\downarrow)|_{\text{pre}}$, which localizes the state to below the initial coherent spin-state level, producing a squeezed state. The same projection is then measured a second time with the final measurement outcome labelled $J_{z\text{f}} = \frac{1}{2}(N_\uparrow - N_\downarrow)|_{\text{fin}}$. The quantum fluctuation is common to both measurements and can be partially subtracted by considering the difference $J_{z\text{d}} = J_{z\text{f}} - J_{z\text{p}}$, but any rotation of the state (that is, signal) that occurs in the interim appears only in the final measurement outcome. Each final population measurement is made after first optically pumping atoms in $|\uparrow\rangle$ to $|F=2, m_F=2\rangle$ to achieve lower readout noise (estimated at more than 15 dB below the projection noise level) by using the optical cycling transition to $|F=3, m_F=3\rangle$.

The length of the Bloch vector J_z after the pre-measurement is measured by inserting a $\pi/2$ pulse between the pre- and final measurements



$$\hat{H}_{\text{OAT}} = \hbar \chi_{\text{OAT}} \hat{J}_z^2 \quad (3)$$

Fig. 3 | Momentum squeezing via OAT and QND measurements. **a**, Probe frequency setup for OAT and QND measurements. During OAT, the laser is fixed at a detuning from cavity resonance δ_p , QND measurements are made by sweeping the probe laser frequency over cavity resonance and detecting the Q quadrature of the reflected field^{5,47}. **b**, QND probe sweeps measured in homodyne and normalized to the full reflected field on resonance I_0 , shown for the empty cavity (grey) and for 900 atoms in $|\uparrow\rangle$ (green). The observed frequency shift enables us to measure the collective population operator \hat{N}_\uparrow with measurement outcome N_\uparrow , without knowing which atoms are in $|\uparrow\rangle$. The probe is sweeping 1.5 MHz ms^{-1} and the atom-cavity detuning is $\delta_c = 2\pi \times 175 \text{ MHz}$. Free-space scattering of probe light results in a slight broadening and reduced amplitude of the observed signal⁴⁷. **c**, QND measurements are used to pre-measure the quantum noise in the spin projection J_z and subtract it from a final measurement as in ref. 5. Increasing the number of probe photons M_i results in a more precise pre-measurement, but at too high of a photon number free-space scattering causes shortening of the Bloch vector (top) and spontaneous Raman scattering to other states. Squeezing is characterized by the spectroscopic enhancement W (bottom) which reaches an optimum below the SQL at $M_i = 600$ photons. Data are fit with 68% confidence bands and all error bars reported are 1σ uncertainties. **d**, State tomography⁵ was performed by applying a variable-duration pulse with rotation axis aligned with the Bloch vector to reconstruct the spin-momentum quasiprobability distributions in the J_y - J_z plane for a coherent spin state (CSS), a QND-squeezed state and an OAT-squeezed state.

(Methods). Specifically, J_s is estimated from the fringe amplitude of $J_{z\uparrow}$ versus the azimuthal phase ϕ of the $\pi/2$ pulse as it is varied between 0 to 2π . The initial length of the Bloch vector J_c needed for estimating the spectroscopic enhancement is estimated in the same manner, but without the pre-measurement applied.

Figure 3c shows the spectroscopic enhancement W versus the strength of the QND interaction as parameterized by M_i , the average number of incident photons that enter the cavity during each population pre-measurement window. At low M_i , the probe's vacuum noise limits the spectroscopic enhancement, whereas at high M_i , the spectroscopic enhancement is limited by free-space scattering of the probe light that leads to a reduction in J_s and transitions to other ground states that decorrelate the pre- and final measurements. Near $M_i = 600$, $N = 1,170(30)$ atoms, and $\delta_c = 2\pi \times 175 \text{ MHz}$, we achieve $W = 0.46(11)$ or $3.4^{+1.1}_{-0.9}$ dB of directly observed squeezing in the momentum-spin basis.

We also realize entanglement by cavity-mediated interactions^{14,43,48}. The OAT Hamiltonian¹

is generated by applying a fixed frequency drive tone offset from the average dressed cavity resonance by $\delta_p \geq \kappa/2$ (ref. 52). In brief, the populations in each momentum-spin state tune the cavity closer to or further from resonance with the fixed frequency drive tone, allowing more or less light into the cavity such that $\hat{c}^\dagger \hat{c} \propto \hat{N}_\uparrow$. To a first approximation, the spin-light QND Hamiltonian is thus transformed into a spin-only Hamiltonian with a relevant term proportional to \hat{N}_\uparrow^2 . A repeated application of the dynamics after a π pulse realizes the Hamiltonian dynamics of equation (3).

The unitary OAT interactions drive shearing of the atomic quantum noise distribution with a resulting squeezed state minimum noise projection oriented at a small angle α_0 from \hat{z} (Fig. 3d and Fig. 4b(inset)). The state is rotated so that the minimum noise projection is along \hat{z} . The momentum-spin populations are destructively read out as before with measurement outcome labelled $J_{z\uparrow}$. The Bloch vector lengths J_s (J_c) with (without) OAT squeezing are also measured just as for the QND squeezing. We directly observe a spectroscopic enhancement from OAT of $W = 0.56(8)$ or $2.5^{+0.6}_{-0.6}$ dB. The optimal configuration was realized with $M_i \approx 700$ photons, $\delta_c = 2\pi \times 350 \text{ MHz}$, $\delta_p = 2.7 \times \kappa/2$, $\chi_{\text{OAT}} \approx 2\pi \times 10 \text{ Hz}$ and $N = 730(10)$ atoms.

Entangled matter-wave interferometry

We now turn to injecting the prepared entangled state into a matter-wave interferometer with the sequence shown in Fig. 4a. After preparing a squeezed state with OAT, a Raman beam splitter rotation orients the squeezing along \hat{y} . The spin projection J_y will change if a small signal phase ϕ is applied. The orienting of the squeezing is accomplished via a $(\pi/2 + \alpha_0)$ pulse aligned to the atomic Bloch vector along \hat{x} . A relative phase accumulates between the wave packets during a free evolution time T_{evol} , a Raman π 'mirror' pulse is applied, followed by another free evolution time T_{evol} . Finally, a readout $\pi/2$ pulse transfers the signal ϕ and the squeezing into a displacement in the momentum-spin population basis \hat{z} with a measurement outcome $J_{z\uparrow}$. The Bloch vector lengths J_s and J_c are measured in separate experiments with and without OAT applied by scanning the azimuthal phase of the final $\pi/2$ pulse of the interferometer and measuring the fringe amplitude as before (Fig. 4c).

We achieve a directly observed spectroscopic enhancement $W = 1.7^{+0.5}_{-0.5}$ dB beyond the SQL with $N = 660(15)$ atoms as shown in Fig. 4b. Without OAT, the performance of our interferometer is worse than the SQL because of imperfect interferometer contrast $C_i = 2J_c/N_0 \approx 0.9$. We note that the actual phase variance of the squeezed interferometer is improved by $3.4^{+0.9}_{-1.2}$ dB compared with this unsqueezed interferometer (Methods).

Phase sensitivity beyond the SQL was limited to evolution times $T_{\text{evol}} < 0.7 \text{ ms}$ (Fig. 4d). A comparable level of decrease in phase sensitivity was observed in an identical sequence in which all optical Raman pulses were replaced by equivalent microwave pulses, suggesting that the spin degrees of freedom may be responsible for the observed loss in sensitivity. We also observe that if the squeezed spin projection is left in the population basis J_z during the interferometer, then the squeezing persists for several milliseconds. From this, we conclude that the entangled state persists for longer than we can directly confirm.

In the future, the combination of Raman and Bragg techniques demonstrated here would enable the most delicate portion of the interferometer to be operated fully with the two portions of the superposition possessing the same spin label.

To further improve interferometer sensitivity, the entanglement can be combined with large momentum transfer sequences or one could inject the squeezed state into a lattice interferometer to hold the atoms for longer⁵⁰. One could also prepare the entanglement in

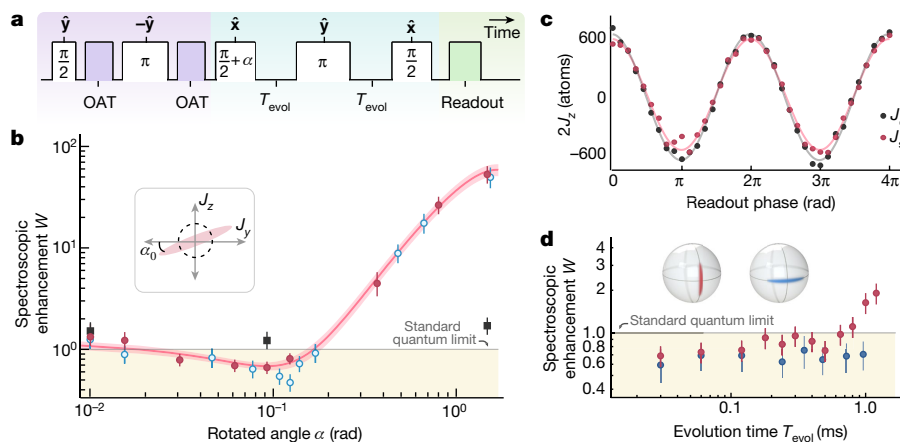


Fig. 4 | Demonstrating sensitivity beyond the SQL. **a**, The squeezed interferometer sequence, including entanglement generation (purple), the interferometer (blue) and state readout (green). Each Raman transition (white) is labelled with magnitude (within) and axis of rotation (above). **b**, The spectroscopic enhancement W is compared for three configurations: a Mach–Zehnder interferometer with OAT (red circles, sequence above), an unentangled interferometer without OAT (black squares) and OAT-squeezed states without the interferometer (blue circles). The duration of a $\pi/2 + \alpha$ rotation is scanned to minimize the projected spin noise at α_0 . To model the Gaussian noise distribution, an ellipse is fit with 68% confidence bands to the

OAT-squeezed interferometer data, giving a minimum variance of $W = 0.68(8)$ or $1.7^{+0.5}_{-0.5}$ dB. The interferometer here had $T_{\text{evol}} = 0.112$ ms and $N = 660(15)$ atoms. **c**, Interferometer contrast fringes with $T_{\text{evol}} = 0.112$ ms shown for no squeezing J_c (black) and with squeezing J_s (red). **d**, Phase sensitivity is maintained below the SQL for the squeezed interferometer (red circles, left Bloch sphere) up to $T_{\text{evol}} = 0.7$ ms. By contrast, if the squeezed spin projection is oriented along the population basis (blue circles, right Bloch sphere), spectroscopic enhancement was seen to persist beyond $T_{\text{evol}} = 1$ ms because this orientation is insensitive to phases accrued during the evolution time. The bias field was 1 G along the cavity axis \hat{Z} for these data. All error bars reported are 1σ uncertainties.

the cavity and allow the atoms to undergo free fall outside of the cavity with readout by fluorescence measurement¹², another promising path for scaling to larger momentum transfers and longer interferometer times. The amount of momentum squeezing could be improved with larger collective cooperativity NC . The need for velocity selection limits our final number of atoms, so higher atom density in momentum space through improved axial cooling or the use of a Bose–Einstein condensate could lead to significant improvements^{34,53–55}. As the atom number is increased, it will be necessary to reduce the level of classical rotation-added noise or to make the added noise common mode as is done for gravity gradiometers and for proposed gravity wave and dark matter detectors^{23–25,56}.

In this work, the OAT-squeezed states were successfully used to realize a squeezed matter-wave interferometer, whereas the QND-squeezed states were not. The OAT produced states were generated at lower atom number and associated smaller momentum spread, leading to less classical added rotation noise relative to the SQL and reduced shortening of the Bloch vector during the rotations. The QND-squeezed states would be enhanced by improving the total effective quantum efficiency from $q \approx 0.1$ here to, for instance, $q \approx 0.4$ in previous work⁵.

It may also be possible to generate spin-squeezed states using optical cycling transitions in rubidium, strontium and ytterbium^{5,10,16,47,51} and then use Raman transitions to map the entanglement to purely momentum states^{42,57}. The fundamental scaling of the achievable Wineland parameter would improve to $W \propto 1/NC$ from the current scaling $W \propto 1/\sqrt{NC}$ (ref. 47). Indeed, the combination of larger atom number and probing on a cycling transition are the primary reasons for the larger amounts of squeezing achieved in previous work^{4,5} compared to the present results.

This proof-of-principle light-pulse matter-wave interferometer paves the way for using cavity-generated entanglement as a quantum resource, enabling the next generation of interferometers with higher precision, enhanced measurement bandwidth, higher accuracy and smaller size. Such devices will advance the frontiers of both practical applications and discoveries in fundamental science.

Online content

Any methods, additional references, Nature Research reporting summaries, source data, extended data, supplementary information, acknowledgements, peer review information; details of author contributions and competing interests; and statements of data and code availability are available at <https://doi.org/10.1038/s41586-022-05197-9>.

- Kitagawa, M. & Ueda, M. Squeezed spin states. *Phys. Rev. A* **47**, 5138–5143 (1993).
- Itano, W. M. et al. Quantum projection noise: population fluctuations in two-level systems. *Phys. Rev. A* **47**, 3554–3570 (1993).
- Wineland, D. J., Bollinger, J. J., Itano, W. M. & Heinzen, D. J. Squeezed atomic states and projection noise in spectroscopy. *Phys. Rev. A* **50**, 67–88 (1994).
- Hosten, O., Engelsens, N. J., Krishnakumar, R. & Kasevich, M. A. Measurement noise 100 times lower than the quantum-projection limit using entangled atoms. *Nature* **529**, 505–508 (2016).
- Cox, K. C., Greve, G. P., Weiner, J. M. & Thompson, J. K. Deterministic Squeezed states with collective measurements and feedback. *Phys. Rev. Lett.* **116**, 093602 (2016).
- Colombo, S. et al. Time-reversal-based quantum metrology with many-body entangled states. *Nat. Phys.* **18**, 925–930 (2022).
- Schleier-Smith, M. H., Leroux, I. D. & Vuletić, V. States of an ensemble of two-level atoms with reduced quantum uncertainty. *Phys. Rev. Lett.* **104**, 073604 (2010).
- Chen, Z., Bohnet, J. G., Sankar, S. R., Dai, J. & Thompson, J. K. Conditional spin squeezing of a large ensemble via the vacuum Rabi splitting. *Phys. Rev. Lett.* **106**, 133 601–133 604 (2011).
- Vasilakis, G. et al. Generation of a squeezed state of an oscillator by stroboscopic back-action-evading measurement. *Nat. Phys.* **11**, 389–392 (2015).
- Bohnet, J. G. et al. Reduced spin measurement back-action for a phase sensitivity ten times beyond the standard quantum limit. *Nat. Photon.* **8**, 731–736 (2014).
- Huang, M.-Z. et al. Self-amplifying spin measurement in a long-lived spin-squeezed state. Preprint at <https://arxiv.org/pdf/2007.01964.pdf> (2020).
- Malia, B. K., Martínez-Rincón, J., Wu, Y., Hosten, O. & Kasevich, M. A. Free space Ramsey spectroscopy in rubidium with noise below the quantum projection limit. *Phys. Rev. Lett.* **125**, 043202 (2020).
- Leroux, I. D., Schleier-Smith, M. H. & Vuletić, V. Orientation-dependent entanglement lifetime in a squeezed atomic clock. *Phys. Rev. Lett.* **104**, 250801 (2010).
- Leroux, I. D., Schleier-Smith, M. H. & Vuletić, V. Implementation of cavity squeezing of a collective atomic spin. *Phys. Rev. Lett.* **104**, 073602 (2010).
- Hosten, O., Krishnakumar, R., Engelsens, N. J. & Kasevich, M. A. Quantum phase magnification. *Science* **352**, 1552–1555 (2016).
- Pedrozo-Peñafiel, E. et al. Entanglement on an optical atomic-clock transition. *Nature* **588**, 414–418 (2020).
- Riehle, F., Kisters, T., Witte, A., Helmcke, J. & Bordé, C. J. Optical Ramsey spectroscopy in a rotating frame: Sagnac effect in a matter-wave interferometer. *Phys. Rev. Lett.* **67**, 177–180 (1991).

18. Peters, A., Chung, K. Y. & Chu, S. Measurement of gravitational acceleration by dropping atoms. *Nature* **400**, 849–852 (1999).
19. Hamilton, P. et al. Atom-interferometry constraints on dark energy. *Science* **349**, 849–851 (2015).
20. Rosi, G. et al. Quantum test of the equivalence principle for atoms in coherent superposition of internal energy states. *Nat. Commun.* **8**, 15529 (2017).
21. Parker, R. H., Yu, C., Zhong, W., Estey, B. & Müller, H. Measurement of the fine-structure constant as a test of the Standard Model. *Science* **360**, 191–195 (2018).
22. Morel, L., Yao, Z., Cladé, P. & Guellati-Khélifa, S. Determination of the fine-structure constant with an accuracy of 81 parts per trillion. *Nature* **588**, 61–65 (2020).
23. Abe, M. et al. Matter-wave Atomic Gradiometer Interferometric Sensor (MAGIS-100). *Quant. Sci. Technol.* **6**, 044003 (2021).
24. Graham, P. W., Hogan, J. M., Kasevich, M. A. & Rajendran, S. New method for gravitational wave detection with atomic sensors. *Phys. Rev. Lett.* **110**, 171102 (2013).
25. Norcia, M. A., Cline, J. R. K. & Thompson, J. K. Role of atoms in atomic gravitational-wave detectors. *Phys. Rev. A* **96**, 042118 (2017).
26. Kroeze, R. M., Guo, Y. & Lev, B. L. Dynamical spin-orbit coupling of a quantum gas. *Phys. Rev. Lett.* **123**, 160404 (2019).
27. Landini, M. et al. Formation of a spin texture in a quantum gas coupled to a cavity. *Phys. Rev. Lett.* **120**, 223602 (2018).
28. Keßler, H. et al. Observation of a dissipative time crystal. *Phys. Rev. Lett.* **127**, 043602 (2021).
29. Schuster, S. C., Wolf, P., Ostermann, S., Slama, S. & Zimmermann, C. Supersolid properties of a Bose-Einstein condensate in a ring resonator. *Phys. Rev. Lett.* **124**, 143602 (2020).
30. Skinner, B., Ruhman, J. & Nahum, A. Measurement-Induced phase transitions in the dynamics of entanglement. *Phys. Rev. X* **9**, 031009 (2019).
31. Kasevich, M. & Chu, S. Atomic interferometry using stimulated Raman transitions. *Phys. Rev. Lett.* **67**, 181–184 (1991).
32. Cronin, A. D., Schmiedmayer, J. & Pritchard, D. E. Optics and interferometry with atoms and molecules. *Rev. Mod. Phys.* **81**, 1051–1129 (2009).
33. Esteve, J., Gross, C., Weller, A., Giovanazzi, S. & Oberthaler, M. K. Squeezing and entanglement in a Bose-Einstein condensate. *Nature* **455**, 1216–1219 (2008).
34. Gross, C., Zibold, T., Nicklas, E., Estève, J. & Oberthaler, M. K. Nonlinear atom interferometer surpasses classical precision limit. *Nature* **464**, 1165–1169 (2010).
35. Bücker, R. et al. Twin-atom beams. *Nat. Phys.* **7**, 608–611 (2011).
36. Hamley, C. D., Gerving, C. S., Hoang, T. M., Bookjans, E. M. & Chapman, M. S. Spin-nematic squeezed vacuum in a quantum gas. *Nat. Phys.* **8**, 305–308 (2012).
37. Luo, X.-Y. et al. Deterministic entanglement generation from driving through quantum phase transitions. *Science* **355**, 620–623 (2017).
38. Lange, K. et al. Entanglement between two spatially separated atomic modes. *Science* **360**, 416–418 (2018).
39. Fadel, M., Zibold, T., Décamps, B. & Treutlein, P. Spatial entanglement patterns and Einstein-Podolsky-Rosen steering in Bose-Einstein condensates. *Science* **360**, 409–413 (2018).
40. Leibfried, D. et al. Creation of a six-atom ‘Schrödinger cat’ state. *Nature* **438**, 639–642 (2005).
41. Monz, T. et al. 14-Qubit entanglement: creation and coherence. *Phys. Rev. Lett.* **106**, 130506 (2011).
42. Anders, F. et al. Momentum entanglement for atom interferometry. *Phys. Rev. Lett.* **127**, 140402 (2021).
43. Schleier-Smith, M. H., Leroux, I. D. & Vuletić, V. Squeezing the collective spin of a dilute atomic ensemble by cavity feedback. *Phys. Rev. A* **81**, 021804 (2010).
44. Braverman, B. et al. Near-unitary spin squeezing in ¹⁷¹Yb. *Phys. Rev. Lett.* **122**, 223203 (2019).
45. Shankar, A., Salvi, L., Chiofalo, M. L., Poli, N. & Holland, M. J. Squeezed state metrology with Bragg interferometers operating in a cavity. *Quant. Sci. Technol.* **4**, 045010 (2019).
46. Salvi, L., Poli, N., Vuletić, V. & Tino, G. M. Squeezing on momentum states for atom interferometry. *Phys. Rev. Lett.* **120**, 033601 (2018).
47. Chen, Z., Bohnet, J. G., Weiner, J. M., Cox, K. C. & Thompson, J. K. Cavity-aided nondemolition measurements for atom counting and spin squeezing. *Phys. Rev. A* **89**, 043837 (2014).
48. Borregaard, J., Davis, E. J., Bentsen, G. S., Schleier-Smith, M. H. & Sørensen, A. S. One- and two-axis squeezing of atomic ensembles in optical cavities. *New J. Phys.* **19**, 093021 (2017).
49. Hamilton, P. et al. Atom interferometry in an optical cavity. *Phys. Rev. Lett.* **114**, 100405 (2015).
50. Xu, V. et al. Probing gravity by holding atoms for 20 seconds. *Science* **366**, 745–749 (2019).
51. Cox, K. C., Greve, G. P., Wu, B. & Thompson, J. K. Spatially homogeneous entanglement for matter-wave interferometry created with time-averaged measurements. *Phys. Rev. A* **94**, 061601 (2016).
52. Zhang, Y.-L., Zou, C.-L., Zou, X.-B., Jiang, L. & Guo, G.-C. Detuning-enhanced cavity spin squeezing. *Phys. Rev. A* **91**, 033625 (2015).
53. Wang, Y.-J. et al. Atom Michelson interferometer on a chip using a Bose-Einstein condensate. *Phys. Rev. Lett.* **94**, 090405 (2005).
54. Jo, G.-B. et al. Long phase coherence time and number squeezing of two Bose-Einstein condensates on an atom chip. *Phys. Rev. Lett.* **98**, 030407 (2007).
55. Gebbe, M. et al. Twin-lattice atom interferometry. *Nat. Commun.* **12**, 2544 (2021).
56. Canuel, B. et al. Exploring gravity with the MIGA large scale atom interferometer. *Sci. Rep.* **8**, 14064 (2018).
57. Jaffe, M., Xu, V., Haslinger, P., Müller, H. & Hamilton, P. Efficient adiabatic spin-dependent kicks in an atom interferometer. *Phys. Rev. Lett.* **121**, 040402 (2018).

Publisher’s note Springer Nature remains neutral with regard to jurisdictional claims in published maps and institutional affiliations.



Open Access This article is licensed under a Creative Commons Attribution 4.0 International License, which permits use, sharing, adaptation, distribution and reproduction in any medium or format, as long as you give appropriate credit to the original author(s) and the source, provide a link to the Creative Commons license, and indicate if changes were made. The images or other third party material in this article are included in the article’s Creative Commons license, unless indicated otherwise in a credit line to the material. If material is not included in the article’s Creative Commons license and your intended use is not permitted by statutory regulation or exceeds the permitted use, you will need to obtain permission directly from the copyright holder. To view a copy of this license, visit <http://creativecommons.org/licenses/by/4.0/>.

© This is a U.S. Government work and not under copyright protection in the US; foreign copyright protection may apply 2022

Blue-detuned doughnut dipole guide

The blue dipole guide laser is a 760 nm interference filter external cavity diode laser (ECDL) locked to a reference cavity for improved long-term stability. The laser is modulated by a fibre electro-optic phase modulator (EOM) with modulation index $\beta \approx 1.3$ at the cavity free spectral range ω_{FSR} . By exciting adjacent longitudinal modes of the cavity with opposite spatial parity with respect to the centre of the cavity, one creates an axially uniform blue dipole guide near the centre of the cavity⁵¹. The doughnut-mode LG_{01} profile is constructed from the \pm first diffraction orders of a fork-pattern phase plate. Stress-induced birefringence of the cavity mirrors breaks cylindrical symmetry and splits the Hermite–Gaussian HG_{10} and HG_{01} modes up to $\delta_{\text{HG}} = 2\pi \times 100\text{--}500$ kHz, depending on the cavity piezo voltage, to be compared with the 157(5) kHz full-width half-maximum cavity linewidth for these modes. For the data presented here, $\delta_{\text{HG}} = 2\pi \times 350$ kHz. Before entering the cavity, the two LG modes are sent along separate paths. One path enters a free-space EOM to generate sidebands for locking the cavity to the blue dipole guide laser. The other path passes through two acousto-optic modulators (AOMs) with a δ_{HG} frequency difference such that the projected HG modes combine within the cavity to approximate an LG_{01} mode's radial intensity distribution by $\text{LG}_{01} = \text{HG}_{01} + i\text{HG}_{10}$. Because the frequency splitting δ_{HG} is much greater than the radial trap frequency, the atoms effectively experience the time-averaged radial trapping potential of an LG_{01} mode.

Laser cooling

The experimental sequence is repeated every 750 ms. Each trial begins with a two-dimensional magneto-optical trap (MOT) loading a three-dimensional MOT with 10^8 atoms near the cavity centre for approximately 0.5 s. The MOT coils are turned off, and around 2×10^5 atoms are cooled by polarization gradient cooling to 15 μK and loaded into an 813.5 nm red-detuned intracavity lattice with full-width half-maximum cavity linewidth 166(5) kHz. Additional radial confinement is provided by the blue dipole guide. The red lattice depth is ramped down to a depth of 80 μK or $250E_r$, where E_r is the recoil energy of the lattice. We then apply Λ -enhanced grey molasses cooling. Each of the six molasses beams has 2.5 mW and 1 cm beam waist. The light is detuned $2\pi \times 42$ MHz blue of $|F=2\rangle \rightarrow |F'=2\rangle$. A fibre EOM generates a 100 μW sideband to coherently form the Λ system as $|F=1\rangle \leftrightarrow |F'=2\rangle \leftrightarrow |F=2\rangle$. After 5 ms, the temperature of the ensemble is reduced to 6 μK .

We then perform two-dimensional degenerate Raman sideband cooling (RSBC) to further cool the radial temperature⁵⁸. Three RSBC beams form a triangular lattice in a plane perpendicular to the cavity axis \hat{Z} , with trapping frequency $\omega_{\text{tri}} = 2\pi \times 75$ kHz. The blue dipole guide and red lattice continue to provide a background radial trap. The RSBC laser is blue-detuned 50 GHz from the $|F=1\rangle \leftrightarrow |F'=2\rangle$ transition so that atoms are trapped at the nodes of the triangular lattice, suppressing scattering off the cooling beams. A bias magnetic field of 0.11 G along \hat{Z} is applied to match the first-order Zeeman splitting to the trap frequency ω_{tri} . The polarizations of the three beams are twisted 10° from the vertical to create the Raman coupling for driving the vibrational mode transition $|F=1, m_F, n_{\text{tri}}\rangle \rightarrow |F=1, m_F - 1, n_{\text{tri}} - 1\rangle$ that reduces the vibrational quantum number n_{tri} in the local traps. During RSBC, atoms are continuously repumped back to $|F=1, m_F = 1\rangle$ by a separate laser.

To improve the coupling of the atoms to the cavity we apply multiple cooling cycles each lasting 2 ms. The RSBC light is ramped on over 0.3 ms, cooling occurs for 1.2 ms and then RSBC light is ramped off over 0.3 ms. After 225 μs , the atoms have oscillated back to the centre of the cavity, at which point we repeat the cooling cycle. After three cooling cycles, we slowly turn off the remaining red lattice and the RSBC lattice over 3 ms so that the atoms start to free fall. Atoms are then optically pumped to $|\uparrow\rangle$ using a pair of π -polarized laser beams

on resonance with the $|F=1\rangle \rightarrow |F'=2\rangle$ and $|F=2\rangle \rightarrow |F'=2\rangle$ transitions applied transverse to the cavity axis. Just before the interferometer sequence, the radial temperature is 1.4(5) μK . State transfer with a microwave pulse may be used for future improvement to reduce heating associated with optical pumping.

Atomic and cavity probe lasers

To stabilize the frequencies of the Raman lasers and the atomic probe relative to the cavity, we frequency lock a separate cavity probe laser to the cavity and then perform offset frequency phase locks to this laser. The cavity probe is locked to a cavity TEM_{00} mode approximately 160 GHz to the blue of the atomic transition frequency ω_a such that this mode is essentially unperturbed by the presence of atoms. The locking of the cavity probe to the cavity is done by a Pound–Drever–Hall lock at very low phase modulation index for a single sideband to carrier power ratio of 10^{-4} . Rather than locking to the carrier, we lock to the weak sideband. This enables us to reduce the amount of power entering the cavity to only 400 pW (half from the sideband and half non-resonantly from the carrier) while still operating above the technical noise floor of the photodiode. This lock is always engaged. To allow phase locking of other lasers to the cavity probe with relative beat notes of less than 2 GHz, some of the laser light is passed through a fibre EOM driven strongly at 13.6 GHz to generate very high order sidebands.

The atomic probe laser is phase-locked with an offset frequency of approximately $13.6 \times 12 = 163.2$ GHz to the red of the cavity probe, placing it close to ω_a . The offset phase-lock frequency is adjusted to maintain the atomic probe laser approximately $\delta_c/2\pi + 80$ MHz blue of ω_a . We derive three important tones from this laser: a homodyne reference beam, a path length stabilization beam used for removing path length noise and drift, and the actual atomic probe tone used for OAT and QND measurements. The path length stabilization beam is passed through an EOM that is modulated at 80 MHz to create a weak sideband that will serve as the atomic probe tone. The combined path length stabilization and atomic probe tones are reflected from the cavity and detected on a single homodyne detector. The homodyne reference beam is shifted by an 80 MHz AOM to have the same frequency as the atomic probe tone. The quadrature of the atomic probe tone that we detect in the homodyne is actively stabilized by adjusting the phase of the homodyne reference tone. This is achieved by detecting the phase of the path length stabilization tone appearing in the homodyne detector at 80 MHz and then holding this phase constant by feedback on the frequency of the 80 MHz AOM used to shift the homodyne reference beam.

The laser could be actively locked to the dressed resonance as in ref.⁵ or the linear part of the dispersive could be used to estimate small frequency shifts, but for this work we sweep the atomic probe laser, and all derived beams, so that the atomic probe tone sweeps through cavity resonance at 1.5 MHz ms^{-1} . Although this simplifies the experiment, it results in a 6 dB loss of quantum efficiency for a fixed amount of free-space scattering when compared to performing homodyne detection on the line centre. Including this loss of efficiency, the net effective quantum efficiency is approximately 10%.

When using the atomic probe to drive OAT, it is ideal to operate with the driving laser detuned from cavity resonance by $\delta_p = \kappa/2$ to suppress free-space scattering. However, we work at larger detunings for two reasons. First, an increased detuning reduces deleterious QND interactions (or, equivalently, photon shot noise from the applied drive tone) that were neglected in our description of the emergence of the unitary dynamics⁵². Second, this enables operation in a linearized regime even in the presence of shot-to-shot total atom number fluctuations. We empirically find an optimum detuning of $\delta_p = 2.7 \times \kappa/2$ with $\chi_{\text{OAT}} \approx 2\pi \times 10$ Hz.

The cavity probe, atomic probe and Raman lasers are distributed-Bragg-reflector lasers with free-running linewidths of approximately

500 kHz. We use external optical feedback to narrow their linewidths⁵⁹. A small fraction of the power from each laser is picked off and then retro-reflected back into the laser with a round trip length of 3 m in free space. The frequency of each laser is primarily determined by the length of the optical feedback path length which is stabilized using a piezo-electric actuator to move the retro-reflection mirror and a free-space phase modulator EOM for fast actuation with unity gain frequency of 500 kHz. By optimizing the optical feedback fraction typically between 10^{-4} and 10^{-3} , we achieve Lorentzian linewidths of less than 1 kHz.

Microwave source

High-fidelity Raman pulse sequences require agile control of low-phase noise microwaves. Our microwave source is based on that in ref.⁶⁰. A low-phase-noise 100 MHz crystal oscillator (Wenzel ULN 501-16843) is multiplied to 6.800 GHz using a non-linear transmission line frequency comb generator (Picosecond Pulse Labs LPN7110-SMT). The stable 6.800 GHz is provided as the local oscillator for a single sideband modulator (Analog Devices HMC496).

The required in-phase I and quadrature Q modulation inputs to the single sideband modulator are created using three radio-frequency (RF) tones from an Analog Devices AD9959 DDS. Two RF tones are at the same frequency near 135 MHz and are 90° out of phase. The phase, frequency and amplitude of these two tones can be jumped for arbitrary rotations on the Bloch sphere, for selecting different momentum-changing transitions, velocimetry and so on. The third RF tone starts near 100 MHz but is continuously ramped in frequency at a rate of $2kg_{\parallel} \approx 2\pi \times 25.1 \text{ kHz ms}^{-1}$ to match the time variation of the two-photon Doppler shift as the atoms fall under gravity. Each of the two initial RF tones are mixed with this third signal to generate tones near 35 MHz for the I and Q inputs to the single sideband modulator.

Finally, the modulator output near 6.835 GHz is divided in frequency by two using a low-noise divider (Analog Devices HMC862A) and applied to a fibre-coupled EOM to generate the desired Raman tones as the \pm first-order sidebands. We estimate that the noise contributed by this frequency source is at least 30 dB below the SQL for 1,000 atoms.

Raman transitions and velocity selection

The laser that drives the Raman transitions is detuned $\Delta = 2\pi \times 85 \text{ GHz}$ blue of ω_a . As is done for the atomic probe, the Raman laser is stabilized with respect to the cavity by an offset frequency phase lock to the cavity probe. The offset frequency is set to centre the Raman laser between two adjacent longitudinal TEM_{00} cavity modes. The two Raman tones, whose generation is described above, are symmetrically detuned from the cavity resonances by approximately $(\omega_{\text{HF}} - \omega_{\text{FSR}})/2 = 2\pi \times 23 \text{ MHz}$. With 2.5 mW of total σ^+ -polarized light incident on the cavity, the EOM modulation index allows a maximum observed two-photon Rabi frequency of $\Omega_{\text{TwoPh}} = 2\pi \times 15 \text{ kHz}$, with the Rabi frequency tuned to smaller values by adjusting the total incident power using an AOM. For the large momentum transfers shown in Fig. 2e, Bragg transitions are driven by two laser tones derived from the same laser with difference frequency $\omega_B = \delta_{\text{vs}} - b(t - t_{\text{vs}})$, where b is the chirp rate defined below.

As atoms fall under gravity, the relative Doppler shift for light propagating upwards versus downwards chirps linearly in time. We compensate for this effect by linearly ramping the instantaneous frequency of the sidebands as $2\omega_R = \omega_{\text{HF}} + \delta - b(t - t_{\text{vs}})$ with chirp rate $b = 2\pi \times 25.11 \text{ kHz ms}^{-1} \approx 2kg_{\parallel}$. Here $g_{\parallel} = 9.8 \text{ m s}^{-2}$ is the projection onto the cavity axis of the local acceleration due to gravity, δ is the two-photon detuning in the falling frame of reference and t_{vs} is the time at which we will apply the first π pulse for velocity selection described below. We also note that during rotation pulses, we adjust the two-photon detuning δ by approximately 4 kHz (in a phase coherent manner) to compensate for differential a.c. Stark shifts of the two pseudospin states induced by the Raman beams. In the accelerating reference frame, the phase of the interferometer fringe evolves quadratically with T nominally as $\phi = (2kg_{\parallel} - b)T^2$, from which we extract

a value of g_{\parallel} consistent with the known local value of gravitational acceleration to within the uncertainty of the angular orientation of the cavity axis with respect to local gravity. The chirp rate b is nominally tuned so that much less than 1 rad of phase evolves in the accelerating frame but, in the laboratory frame, the accumulated phase evolves as $\phi = 2kg_{\parallel}T^2$, which is approximately 2,500 rad for the largest $T = 4 \text{ ms}$ explored in this work.

After being released from the 813 nm lattice and falling for $T_{\text{fall}} = 15 \text{ ms}$, the atoms are optically pumped to $|\uparrow\rangle$, and the two-photon Raman detuning is set to $\delta_{\text{vs}} = -2\pi \times 400 \text{ kHz} \approx bT_{\text{fall}}$ to transfer a group of atoms to $|\downarrow\rangle$ from the centre of the axial velocity distribution⁶¹. Atoms in $|\uparrow\rangle$ are removed by a transverse radiation pressure force. The velocity selection is then repeated to further narrow the momentum width of the selected atoms down to $\Delta p < 0.1\hbar k$ set by the two-photon Rabi frequency $\Omega_{\text{TwoPh}} = 2\pi \times 1.4 \text{ kHz}$.

The Raman laser is a distributed-Bragg-reflector laser with a free-running linewidth of approximately 500 kHz. We observed that the cavity converted laser frequency noise to intracavity amplitude noise near δ_{vs} that can resonantly drive undesired Bragg transitions, leading to a loss of nearly 50% of the population to other momentum states outside of the desired two-level basis for all the Raman pulses involved in the interferometer sequence combined. We note that in the symmetric detuning configuration here the Raman transitions are first-order insensitive to conversion of laser frequency noise to both amplitude (AM) and phase (PM) noise on the intracavity Raman tones. However, the Bragg transitions are first-order sensitive because of the opposite parity of the standing wave modes being driven.

After narrowing the laser to a Lorentzian linewidth of less than 1 kHz, we found the fraction of total atoms lost out of the desired two-level manifold is less than 3(3)% for all the Raman pulses involved in the interferometer sequence combined. We also observed residual off-resonance transitions to other momentum states if the turn on and off of the Raman beams was too rapid. The fraction of atoms lost per pulse was reduced to 0.2(1.0)% per pulse by using an RF switch with 3 μs rise time to gate the Raman tones. Without the shortening of the Bloch vector J_c from the two effects, we estimate that the observed spectroscopic enhancement could be improved by 0.2(2) dB for the full interferometer sequence.

Wineland criterion

The Wineland criterion is often presented in the form⁵

$$W = \frac{(\Delta J_z)^2 C_i}{\Delta J_{z,\text{SQL}}^2 C_f^2}, \quad (4)$$

where the initial C_i and final C_f contrasts are related to Bloch vector lengths here by $C_i \equiv 2J_c/N_0$ and $C_f \equiv 2J_c/N_0$ for total atom number N_0 . By rearranging terms, it can also be expressed in a more physically meaningful form as the ratio $W = (\Delta\theta/\Delta\theta_{\text{SQL}})^2$ between the observed angular resolution $\Delta\theta = \frac{\Delta J_z}{J_c}$ with entanglement and the SQL $\Delta\theta_{\text{SQL}} = 1/\sqrt{N} \equiv 1/\sqrt{2}J_c$ for a pure state with the same Bloch vector length J_c as that of the actual mixed state when entanglement is not created.

We now establish the connection between the spin operators and actual experimental measurements. We define the cavity frequency shifts induced by a single atom in $|F=2, m_F=2\rangle$, $|F=2, m_F=0\rangle$ and $|F=1, m_F=0\rangle$ as $\chi_2, \chi_0 \equiv \chi_{\text{QND}}$ and χ_1 , respectively.

For OAT squeezing, we estimate the angular resolution $\Delta\theta$ after the squeezing generation or the full squeezed interferometer sequence as follows. To measure the final spin projection $J_{z\text{f}}$, we optically pump the atoms in $|\uparrow\rangle$ to $|F=2, m_F=2\rangle$, measure the cavity frequency shift with outcome labelled $\omega_{1\text{f}}$, blow away atoms in $|F=2\rangle$, apply a Raman π pulse, optically pump the atoms in $|\uparrow\rangle$ to $|F=2, m_F=2\rangle$ and measure a second cavity frequency shift with outcome labelled $\omega_{2\text{f}}$. We estimate the final spin projection $J_{z\text{f}}$ from the difference between the two cavity frequency shifts $J_{z\text{f}} = \frac{\omega_{1\text{f}} - \omega_{2\text{f}}}{2\chi_2} - \frac{e}{\chi_2} \omega_{2\text{f}}$, where $e = \frac{\chi_1/\chi_2}{\chi_2}$. To convert the spin projection

Article

J_{zf} into an estimate of the Bloch vector polar angle θ_p , we measure the length of the Bloch vector J_s by scanning the azimuthal phase ϕ of the readout $\pi/2$ pulse. In the case of the squeezed interferometer, this is the final $\pi/2$ pulse of the interferometer and just before the measurement J_{zf} . In the case of OAT-squeezed state generation, this is an added $\pi/2$ pulse after the squeezing and just before the measurement J_{zf} . We fit the resulting differential cavity frequency shifts $(\omega_{1f} - \omega_{2f})|_{\phi}$ to the function $y_0 + A_f \sin(\phi - \phi_0)$ with fitted offset y_0 , amplitude A_f and phase offset ϕ_0 . The Bloch vector length is then estimated by $J_s = \frac{A_f}{2\chi_2 - \chi_1}$. The Bloch vector polar angle θ_f from the final measurement is thus estimated by $\theta_f = \frac{J_{zf}}{J_s} = \frac{\omega_{1f} - \omega_{2f}}{A_f} - e^{\frac{\omega_{1f} + \omega_{2f}}{A_f}} + 2e^{\frac{2\omega_{2f}}{A_f}}$.

The angular resolution $\Delta\theta$ is approximated as $\Delta\theta = \Delta\theta_f \approx \frac{\Delta(\omega_{1f} - \omega_{2f})}{A_f}$, where we note the scale factors χ_2 , and so on, are cancelled at the order of ϵ^0 . With a typical value of $|\epsilon| < 1/50$ and the fractional total number fluctuation $\Delta\left(\frac{\omega_{1f} + \omega_{2f}}{A_f}\right)$ being less than 0.03, the corrections of order ϵ^1 would need to be included for squeezing 30 dB below the SQL.

For the QND measurements, we perform pre-measurements to localize the quantum state and use the final measurements to verify the squeezing generated by the pre-measurements as described before. The phase resolution is defined as the phase fluctuation between the pre- and final measurements $\Delta\theta = \Delta(\theta_p - \theta_f)$. The Bloch vector polar angle of the final measurements θ_f is estimated as in the OAT measurement with the atomic population optically pumped to $|F=2, m_F=2\rangle$. For the pre-measurements, we measure pairs of cavity frequency shifts ω_{1p} and ω_{2p} separated by π pulses but without the optical pumping so the atomic population is in $|\uparrow\rangle$ during the cavity frequency shift measurements. The spin projection J_{zp} in the pre-measurements is estimated from the differential frequency shift $J_{zp} = \frac{\omega_{1p} - \omega_{2p}}{2(\chi_0 - \chi_1)}$. The length of the Bloch vector J_s just after the pre-measurement is measured by adding a $\pi/2$ pulse just after the pre-measurement and scanning its azimuthal phase ϕ , after which we perform a single cavity frequency shift measurement with outcome labelled $\omega_{1f}|_{\phi}$. We then fit the resulting fringe to the function $y_0 + A_p \sin(\phi - \phi_0)$ and estimate the Bloch vector length $J_s = \frac{A_p}{\chi_0 - \chi_1}$. The Bloch vector polar angle θ_p is evaluated $\theta_p = \frac{J_{zp}}{J_p} = \frac{\omega_{1p} - \omega_{2p}}{2A_p}$. As before, the angular phase resolution is sufficiently approximated by keeping only to the order of ϵ^0 as $\Delta\theta = \Delta(\theta_p - \theta_f) \approx \Delta\left(\frac{\omega_{1p} - \omega_{2p}}{2A_p} - \frac{\omega_{1f} - \omega_{2f}}{A_f}\right)$ with no dependence on scale factors χ_2, χ_0 or χ_1 .

For estimating the SQL $\Delta\theta_{SQL}$, we measure the length of the Bloch vector $J_c = J_s|_{M_f=0} = \frac{A_{pl}M_f=0}{\chi_0 - \chi_1}$ using the same sequence for measuring J_s in the QND pre-measurements described just above but setting the photon number M_f to zero during the pre-measurements or squeezing for QND measurement or OAT, respectively. To estimate the SQL $\Delta\theta_{SQL} = 1/\sqrt{N} = 1/\sqrt{2J_c}$ we therefore need to know accurate values of χ_0 and χ_1 . To sufficient approximation $\chi_0 = g^2 \left(\frac{B_3}{\delta_c} + \frac{B_2}{\delta_c + \delta_2} + \frac{B_1}{\delta_c + \delta_1} \right)$ with atom-cavity coupling g discussed below, hyperfine splittings $\delta_2 = 2\pi \times 266.7$ MHz, $\delta_1 = 2\pi \times 423.6$ MHz and branching ratios $B_3 = \frac{6}{15}$, $B_2 = \frac{3}{12}$, $B_1 = \frac{1}{60}$ of the excited states $|F'=3, 2, 1, m_F=1\rangle$ to the ground-state $|\uparrow\rangle$ transition that interact with the probe light. To an sufficient approximation, $\chi_1 = g^2 \left(\frac{B_{2,\downarrow}}{\delta_c + \delta_2 - \omega_{HF}} + \frac{B_{1,\downarrow}}{\delta_c + \delta_1 - \omega_{HF}} \right)$ with branching ratios $B_{2,\downarrow} = \frac{3}{12}$, $B_{1,\downarrow} = \frac{5}{12}$ of the $|F'=2, 1, m_F=1\rangle$ to the ground-state $|\downarrow\rangle$ transition. Although not used in the calculation, the cavity frequency shift from a single atom in $|F=2, m_F=2\rangle$ is approximated by $\chi_2 = \frac{g^2}{\delta_c}$ for the cycling transition between the excited state $|F=3, m_F=3\rangle$ and the ground state $|F=2, m_F=2\rangle$.

The maximum single-atom vacuum Rabi splitting $2g_0 = 2\sqrt{\frac{2D^2\omega_c}{\pi L\omega_0^2\epsilon_0\hbar}} = 2 \times 2\pi \times 0.4853(5)$ MHz (ref. ⁷), with fractional uncertainty dominated by the fractional uncertainty (1.1×10^{-3}) on the dipole matrix element D for the $|F=2, m_F=2\rangle$ to $|F=3, m_F=3\rangle$ transition, and ϵ_0 the vacuum permeability. The cavity length L and mode waist ω_0 are determined very precisely by measuring the free spectral range and transverse mode frequency splitting. As the atoms traverse many standing waves of the cavity during the measurement windows, we can average over

the standing waves to arrive at a time-averaged spatially dependent coupling $g_t(r, z) = \frac{g_0}{\sqrt{2}} \frac{e^{-r^2/w_0^2}}{\sqrt{1 + \left(\frac{z}{Z_R}\right)^2}}$, where $Z_R = 2.1$ cm is the Rayleigh range

of the cavity⁵¹. The effective single-atom-cavity coupling frequency is given by the ensemble averaged moments of the spatially dependent $g_t(r, z)$ as $g = \sqrt{\frac{\langle g_t(r, z)^4 \rangle}{\langle g_t(r, z)^2 \rangle}} = \frac{g_0}{\sqrt{2}} (1 - f_{cor}) = 2\pi \times 0.341(2)$ MHz (ref. ⁷). The final fractional uncertainty (6×10^{-3}) on g is dominated by the uncertainty on the correction factor $f_{cor} \approx \frac{z_0^2 + \sigma_z^2}{2Z_R^2} + \frac{r_{r.m.s.}^2}{w_0^2}$, where $z_0 = 1(2)$ mm is the axial position of the cloud relative to the cavity centre, $\sigma_z = 0.5(3)$ mm is the r.m.s. axial spread of the cloud and $r_{r.m.s.}$ is the r.m.s. cloud radius of the atoms. The fractional uncertainty on g contributed from z_0, σ_z and $r_{r.m.s.}$ are 5×10^{-3} , 4×10^{-3} and 2×10^{-3} , respectively.

The uncertainties on the cavity detuning $\delta_c = 175(2)$ MHz or 350(2) MHz lead to fractional uncertainties of at most 0.01 on $(\chi_{QND} - \chi_1)$. Because the atoms move along the cavity axis, the probe light is Doppler shifted by the order of $\delta_{vs}/2$; however, here $\delta_c \gg \delta_{vs}$ so that there is only a negligible fractional correction to χ_{QND} of order $(\delta_{vs}/2\delta_c)^2 \lesssim 10^{-6}$. The effect of spread in momentum states is even more negligible.

Combining uncertainties from g and δ_c , the fractional uncertainty on $(\chi_{QND} - \chi_1)$ is at most 1.4×10^{-2} . This uncertainty combined with the fractional uncertainty on the fitted fringe amplitude A_p of 9×10^{-3} yields a total fractional uncertainty on the SQL variance $(\Delta\theta_{SQL})^2$ of 1.7×10^{-2} . To estimate the angular resolutions $(\Delta\theta)^2$, we typically use 100 to 200 experimental trials, which leads to a typical statistical fractional uncertainty on $(\Delta\theta)^2$ of 0.1 to 0.2. The final reported uncertainties on the Wineland parameters are thus dominated by the statistical uncertainties on the phase resolution $(\Delta\theta)^2$.

Without the QND pre-measurements or OAT, the mixed state actually performs worse than the SQL, conceptually due to the spin noise from the dephased or decohered fraction of the atoms that contribute noise but no signal. This is why the observed improvement in the interferometer sensitivity is larger than the Wineland parameter; however, the Wineland parameter captures what fraction of the improvement can be certified to arise because of entanglement between the atoms and not just because of cancellation of spin noise alone.

Vibration noise

Mechanical vibrations of the cavity mirrors are equivalent to a fluctuating phase reference for the atoms. A commercial vibrometer was used to measure the spectral density $S_a(\omega)$ of acceleration noise at a location on the optical table close to the portion that supports the vacuum chamber. In the limit of zero-duration pulses, the transfer function for a Mach-Zehnder interferometer $|T(\omega)|^2 = \frac{64k^2}{\omega^4} \sin^2\left(\frac{\omega T_{evol}}{2}\right)$ converts accelerations to an integrated phase noise $\phi^2 = \int_0^\infty |T(\omega)|^2 S_a(\omega) d\omega$. For a sequence with $T_{evol} = 0.3$ ms, we estimate that the phase noise caused by vibrations is 20 dB lower than the phase resolution set by the SQL of 1,000 atoms.

Data availability

The datasets generated during and/or analysed during the current study are available in the CU Scholar repository, with the identifier <https://doi.org/10.25810/t39m-c562>.

58. Vuletić, V., Chin, C., Kerman, A. J. & Chu, S. Degenerate Raman sideband cooling of trapped cesium atoms at very high atomic densities. *Phys. Rev. Lett.* **81**, 5768–5771 (1998).
59. Yamoah, M. et al. Robust kHz-linewidth distributed Bragg reflector laser with optoelectronic feedback. *Opt. Express* **27**, 37714–37720 (2019).
60. Chen, Z., Bohnet, J. G., Weiner, J. M. & Thompson, J. K. A low phase noise microwave source for atomic spin squeezing experiments in ⁸⁷Rb. *Rev. Sci. Instrum.* **83**, 044701 (2012).
61. Kasevich, M. et al. Atomic velocity selection using stimulated Raman transitions. *Phys. Rev. Lett.* **66**, 2297–2300 (1991).

Acknowledgements We acknowledge funding support from the National Science Foundation under grant numbers 1734006 (Physics Frontier Center) and OMA-2016244 (QLCI), DOE Quantum Systems Accelerator, NIST and DARPA. We acknowledge helpful feedback on the manuscript from D. Z. Anderson and A. M. Rey, helpful discussions with M. Jaffe and N. Poli, and laser locking development by D. Wu.

Author contributions G.P.G., C.L. and B.W. contributed to the building of the experiment. G.P.G. and C.L. conducted the experiments and data analysis. J.K.T. conceived and supervised the experiments. G.P.G., C.L. and J.K.T. wrote the manuscript. All authors discussed the experiment implementation and results and contributed to the manuscript.

Competing interests The authors declare no competing interests.

Additional information

Supplementary information The online version contains supplementary material available at <https://doi.org/10.1038/s41586-022-05197-9>.

Correspondence and requests for materials should be addressed to James K. Thompson.

Peer review information *Nature* thanks Maria Luisa Chiofalo, Paul Hamilton and the other, anonymous, reviewer(s) for their contribution to the peer review of this work. Peer reviewer reports are available.

Reprints and permissions information is available at <http://www.nature.com/reprints>.